J Med Ultrasonics (2011) 38:73–80
DOI 10.1007/s10396-011-0298-7

ORIGINAL ARTICLE

Small calcification depiction in ultrasound B-mode images using decorrelation of echoes caused by forward scattered waves

Hirofumi Taki · Takuya Sakamoto · Makoto Yamakawa · Tsuyoshi Shiina · Kenichi Nagae · Toru Sato

Received: 17 September 2010 / Accepted: 14 December 2010 / Published online: 25 February 2011

Abstract
Purpose The purpose of this study is to propose a novel method to depict small calcifications in ultrasound B-mode images using decorrelation of forward scattered waves with no decrease in the frame rate.
Methods Since the waveform of an ultrasound pulse changes when it passes through a calcification location, the echo waveform from regions behind the calcification is quite different from that without a calcification. This indicates that the existence of a calcification is predictable based upon the waveform difference between adjacent scan lines by calculating cross-correlation coefficients. In addition, a high-intensity echo should return from the calcification itself. Therefore, the proposed method depicts the high-intensity echo positions with posterior low correlation coefficient regions.
Results Eleven of 15 wires 0.2–0.4 mm in diameter were depicted using this method, yielding a sensitivity of 73.3% and a specificity of 100%, even though they might go undetected under clinical inspection of ultrasound B-mode images.
Conclusion This study suggests that an US device could perform well in terms of calcification detection.

Keywords Ultrasonography · Calcification · Decorrelation · Forward scattered wave · Calcification detection

H. Taki (✉) · T. Sakamoto · T. Sato
Graduate School of Informatics, Kyoto University, Yoshida-honmachi, Sakyo-ku, Kyoto 606-8501, Japan
e-mail: hirofumi.taki@mb6.seikyou.ne.jp

M. Yamakawa
Advanced Biomedical Engineering Research Unit, Kyoto University, Yoshida-honmachi, Sakyo-ku, Kyoto 606-8501, Japan

T. Shiina
Graduate School of Medicine, Kyoto University, Yoshida-honmachi, Sakyo-ku, Kyoto 606-8501, Japan

K. Nagae
Corporate R&D HQ, Canon Inc, 30-2, Shimomaruko 3-chome, Ohta-ku, Tokyo 146-8501, Japan

Introduction

Ultrasonography (US) has an excellent ability to depict soft tissues without ionizing radiation; however, the calcification detectability of US is insufficient compared with X-ray computed tomography (CT) and other X-ray imaging techniques [1–4]. The detection of calcification is an important factor when diagnosing the malignancy of masses. As such, improvement of the calcification detectability of US is strongly desired.

Since the echo from a calcification is supposed to be of high intensity, several calcification detection methods that use extraction of high-echo-intensity regions have been reported. For extraction of high-echo-intensity regions, many researchers have employed a constant false alarm rate (CFAR) technique [5, 6]. A CFAR detector extracts targets in nonstationary noise and clutter while maintaining a constant probability of a false alarm [7, 8]. Therefore, a small calcification with low echo intensity is almost never detected using CFAR detectors. In addition, when a layered structure exists close to a calcification, the specular echo from the layered structure severely interferes with detection of the calcification.

Other strategies to detect small calcifications employ techniques to suppress speckle artifacts. Tissue harmonic

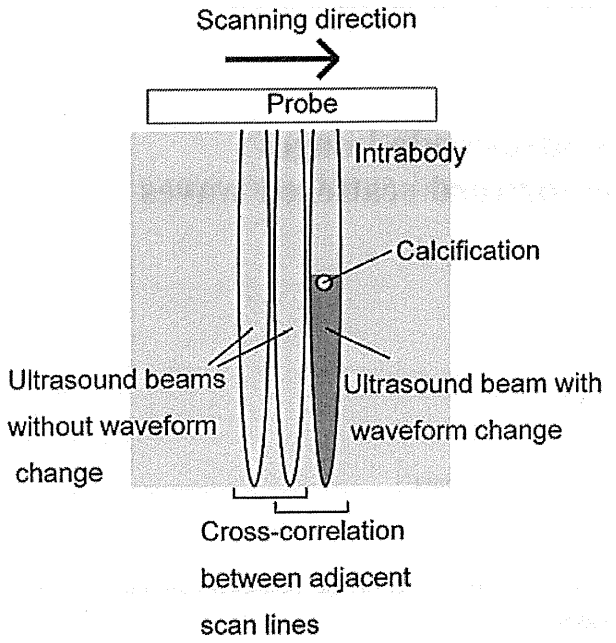

Fig. 1 Schema of the proposed calcification depiction method using correlation coefficients between adjacent scan lines

imaging (THI) utilizes harmonics to suppress speckle artifacts [9–12]. However, THI exhibits considerably lower performance than CT in terms of calcification detection [1]. In contrast, spatial compound imaging generates a single B-mode image from multiple sweeps [13–16]. This causes the suppression of acoustic shadowing, resulting in the low performance of spatial compound imaging for calcification detection [17].

We have proposed a calcification detection strategy using cross-correlation between adjacent scan lines for detection of a small calcification with low echo intensity [18, 19]. Since the acoustic impedance of a calcification is much larger than that of other tissues, the waveform of an ultrasound wave changes significantly when it passes through the calcification location. This causes decorrelation between adjacent scan lines behind the calcification location, as shown in Fig. 1. Therefore, the existence of a calcification is predictable using the region with decorrelation that continues along the range direction, similar to calcification detection using acoustic shadowing. In addition, a relatively high intensity echo returns from a calcification because of its large acoustic impedance mismatch to soft tissue. In this study, we thus propose a method to presume the existence of calcifications by selecting high-echo-intensity positions with posterior low correlation regions. A layered structure behind a calcification improves the performance of the calcification depiction method [18]. Therefore, we investigate the performance of the proposed method experimentally under the condition that a layered structure exists just behind a calcification, which is one of the most difficult cases in which to detect calcifications with US and suitable for the proposed calcification depiction method.

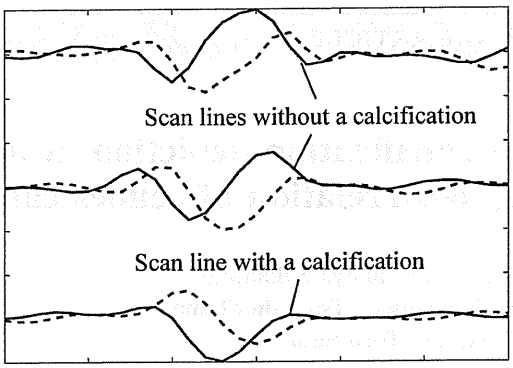

Fig. 2 Waveforms of two scan lines of in-phase and quadrature data without a calcification and one scan line with a calcification. *Solid* and *broken lines* denote the waveforms of in-phase and quadrature data, respectively

Materials and methods

Extraction of high-echo-intensity regions

An echo from a calcification should have a relatively high intensity because of its large acoustic impedance mismatch to soft tissue. For the selection of candidates for calcifications, the proposed method picks up positions where echo intensities exceed an intensity threshold, I_t. The condition of the cutaneous tissue layer influences the echo intensity in a region of interest behind the cutaneous layer. In contrast, two measurement regions of the same tissue have similar distribution shapes in terms of echo intensity. Therefore, the selection of candidates for calcifications should employ a rank filter, not a fixed echo intensity. We thus chose I_t as the intensity of a pixel that is a certain fraction of the maximum intensity value of the pixels in the image. The value of I_t depends on the echo intensity distribution of the measurement tissue, and the user should employ a value of I_t that is adequate to pick up all the pixels with sufficient intensities. In this study, we set I_t as 1% of the maximum intensity value of a pixel in a B-mode image.

Correlation between adjacent scan lines

The proposed method utilizes correlation between adjacent scan lines for the depiction of calcifications. When a calcification exists in a scan line, creeping waves around the calcification surface, diffraction waves, and multiple reflection waves in the calcification occur in both the transmit and receive events. These forward scattered waves change the waveform considerably, as shown in Fig. 2. The

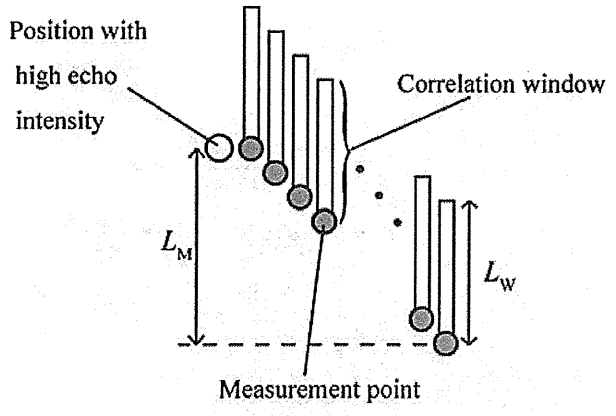

Fig. 3 Measurement points behind a high-echo-intensity position investigated using the proposed method. L_W and L_M denote the correlation window width and the width of the measurement region behind the high-echo-intensity position, respectively

correlation of the echoes behind a calcification is thus suppressed severely. Since a calcification suppresses correlation of the region behind the calcification, the proposed method utilizes the measurement points behind a high-echo-intensity position where the correlation windows of the measurement points include the region behind the high-echo-intensity position, as shown in Fig. 3.

US devices acquire in-phase and quadrature (IQ) data for detection of the Doppler signal, and most devices utilize quadrature detectors for acquisition of IQ data. Detection is accomplished by mixing the received signal with two sinusoidal waves, where the phase difference of the two sinusoidal waves is 90° and their center frequency is equal to the transmit center frequency. A cross-correlation coefficient between adjacent scan lines of IQ data is suppressed not only by the existence of a calcification but also by the noise intensities of the scan lines. We thus employed an echo intensity constraint to suppress the influence of noise. The cross-correlation coefficient with a constraint is given by

$$r\left(x+\frac{\Delta X}{2},z\right) = \max_{L} \frac{\left|\sum_{z'=z-L_W}^{z} g(x,z')g(x+\Delta X,z'+L\Delta Z)^*\right|}{\sqrt{\sum_{z'=z-L_W}^{z}|g(x,z')|^2 \sum_{z'=z-L_W}^{z}|g(x+\Delta X,z'+L\Delta Z)|^2}}, \quad (1)$$

subject to

$$\sqrt{\sum_{z'=z-L_W}^{z}|g(x,z')|^2 \sum_{z'=z-L_W}^{z}|g(x+\Delta X,z'+L\Delta Z)|^2} \geq \alpha m I_t, \quad (2)$$

where x and z are respectively the lateral and vertical components of a measurement point in a B-mode image, $g(x, z)$ is the IQ datum at a pixel in a B-mode image, $g(x, z)^*$ is the complex conjugate of $g(x, z)$, ΔX is the scan line interval, ΔZ is the range interval, α is a positive number employed for the echo intensity threshold, and L_W and m are the width and number of pixels of the correlation window, respectively. The variable L is employed to acquire the maximum of the correlation coefficients. The correlation coefficient is normalized by the average echo intensity, and thus it relates to the waveform change itself. In this study, we examined cases of $\alpha = 0.05$, 0.1, and 0.2. We set the correlation window width, L_w, and the width of the measurement region behind a high-echo-intensity position, L_M, to 5 and 6 mm, respectively. Since the range interval is 0.05 mm, the number of pixels of the correlation window is 100. In the cases of $\alpha = 0.05$, 0.1, and 0.2, the method eliminates the cross-correlation coefficients with the echo intensity under 5, 10, and 20 times the echo intensity threshold, I_t, respectively. Since I_t is the echo intensity of a single pixel with a sufficient intensity, the echo cut out by the correlation window seldom has an echo intensity over 40 times I_t. In contrast, the echo intensity under twice I_t indicates an insufficient signal-to-noise ratio of the echo, and the echo should be eliminated. Therefore, the values of α are adequate, and optimization of the values of α is not necessary.

Depiction of high-echo-intensity positions with posterior low correlation regions

A calcification originates a high-echo-intensity position accompanied by a low correlation region behind the position. Therefore, the present method presumes the calcification positions by selecting the high-echo-intensity positions with posterior low correlation regions. First, the method calculates the ratio of correlation coefficients lower than the value of a correlation threshold among the measurement region behind each high-echo-intensity position. The correlation threshold of $\mu - \beta\sigma$ is determined using the average, μ, and the standard deviation, σ, of the correlation coefficients of all the measurement regions behind all the high-echo-intensity positions, where β is a positive number. Then, the method depicts the high-echo-intensity position with a posterior low correlation region, where the region accounts for half the measurement region behind the high-echo-intensity position. In this study, we examined two cases, i.e., $\beta = 2$ and 3, because they are adequate statistically.

Experimental setup

Experiments were conducted with a Hitachi EUB-8500 (Hitachi, Tokyo, Japan) US device, which has a function to export raw IQ data. A 7.5-MHz linear array probe was used, where the scan line interval, ΔX, and range interval, ΔZ, of the device were 0.13 and 0.05 mm, respectively. We

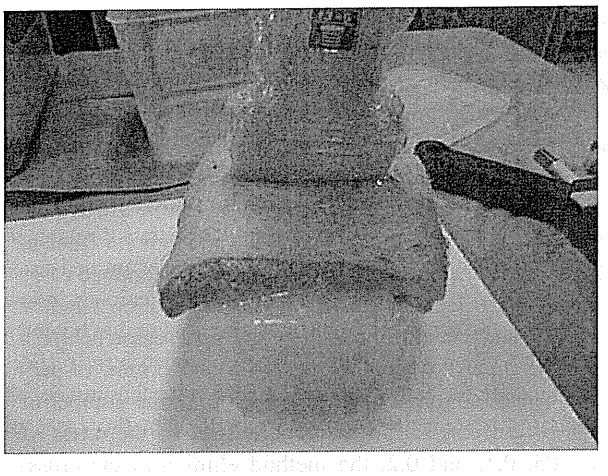

Fig. 4 Calcification phantom prepared in this study

prepared a calcification phantom with three different copper wires (0.2, 0.29, and 0.4 mm in diameter from left to right) embedded into a 4% agar gel block at 2 cm depth and 1 cm intervals, as shown in Fig. 4. A polyethylene sheet 0.1 mm thick was placed just behind the wires. The agar gel contained 0.5% Tech Polymer particles, spherical polymer particles 7 μm in diameter (Sekisui Plastics). Aberrations originating at a cutaneous tissue layer deteriorate the image quality of B-mode images, causing interference of calcification detection. To evaluate the influence of a cutaneous tissue layer, we placed a swine cutaneous tissue layer 1 cm thick onto the gel block. To avoid multiple reflections in the wires, the image plane was set at 85° to the wires. Figure 5 shows a B-mode image of the calcification phantom. In this set up, the specular echo from a polyethylene sheet had a higher intensity than that from wires, indicating that the strategy of selecting high-echo-intensity masses, such as CA CFAR detectors, was unsuitable for small calcification detection. Kamiyama et al. [6] focused on the tissue structure in a B-mode image having continuity in the lateral direction, and they proposed a calcification detection method using CA CFAR with a kernel that emphasizes the lateral direction. The cell averaging process employed by the method calculates the indicator of calcification:

$$P_{\mathrm{CA}}(x, y) = P_{\mathrm{L}}(x, y) - P_{\mathrm{K}}(x, y), \tag{3}$$

where $P_{\mathrm{L}}(x, y)$ is the logarithmic intensity of a measurement pixel, and $P_{\mathrm{K}}(x, y)$ is the average of the logarithmic intensity of the kernel pixels surrounding the measurement pixel. However, the calcification detection ability of the method deteriorates when a layered structure is not parallel to the lateral direction and the echo intensity of the layered structure varies, as shown in Fig. 6.

In the present study, five B-mode images of different sections were obtained. Each B-mode image contained

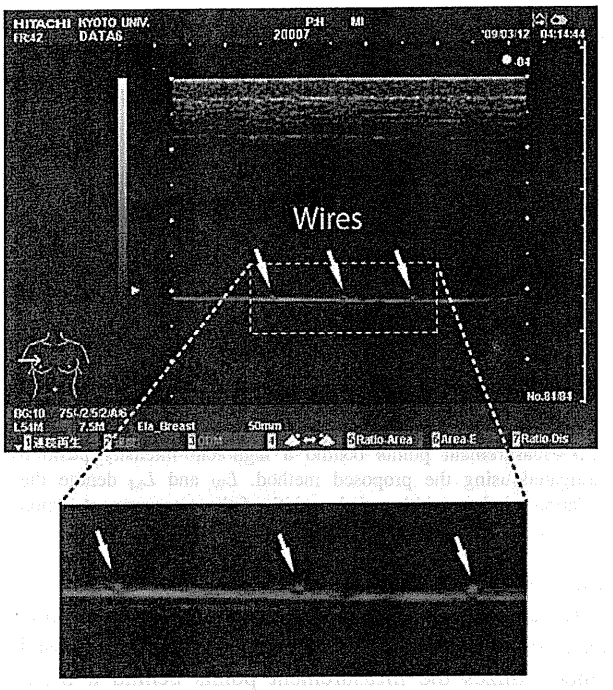

Fig. 5 B-mode image of the calcification phantom with a swine cutaneous tissue layer. *White arrows* point to wires simulating calcifications

three wires, and thus the sum of the embedded wires was 15. To investigate the robustness of the proposed method, we also prepared a calcification phantom without a swine cutaneous tissue layer. As shown in Fig. 7, absence of a swine tissue layer was far from in vivo conditions, and the wires were easily detected upon US inspection.

Results and discussion

Calcification depiction using low correlation of adjacent scan lines

First, the proposed method selects high-echo-intensity positions in a B-mode image of a calcification phantom. As shown in Fig. 8, almost all specular echoes and echoes from wires were picked up by using the 1% intensity threshold. This indicates the validity of the echo intensity threshold for the calcification phantom. Then, the method calculates correlation coefficients in the measurement region behind the high-echo-intensity positions. Figure 9 shows correlation coefficients between adjacent scan lines, where three values of the intensity threshold, α, were examined. The employment of a low value for α means that the method counts scan lines with low SNR among the region for the calculation of correlation coefficients, causing enhancement of the influence of noise on the

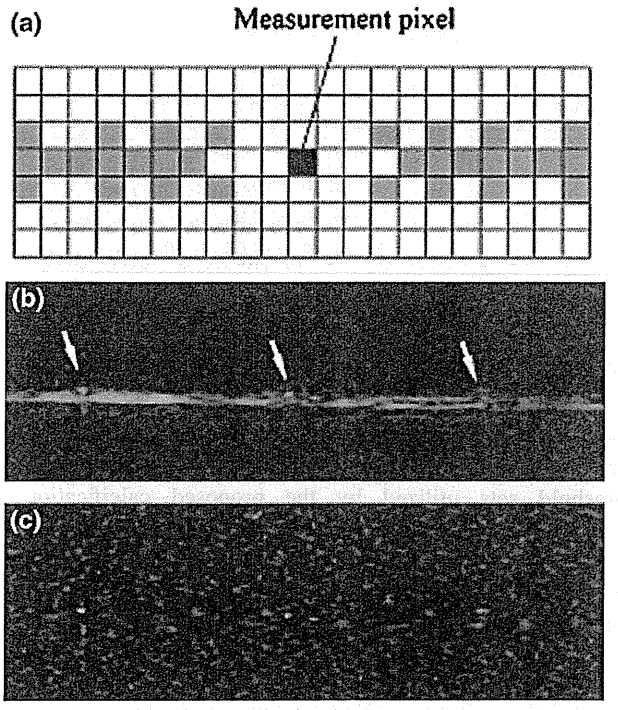

Fig. 6 **a** Kernel pattern that emphasizes the lateral direction [6]. **b** B-mode image of the calcification phantom, and **c** that with the cell averaging process using the kernel. *Gray pixels* denote the kernel pixels, and the *white arrows* point at wires

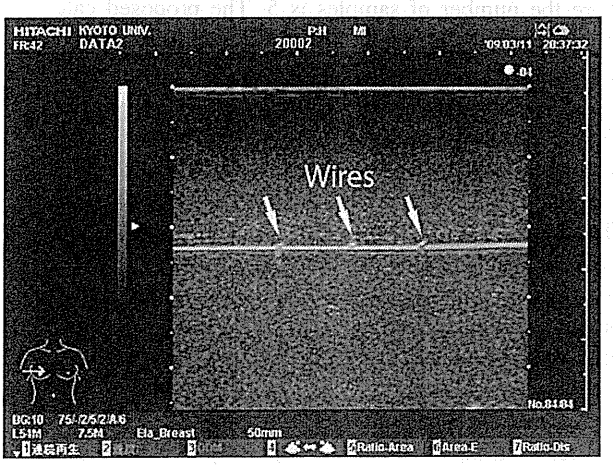

Fig. 7 B-mode image of the calcification phantom without a swine cutaneous tissue layer

correlation profile. When α of 0.05 was employed, correlation coefficients were suppressed continuously along the range direction behind the middle and right wires. When $\alpha = 0.2$ was employed, false images were eliminated and the suppression of correlation coefficients caused by the left wire became conspicuous at a cost of the loss of the low correlation region caused by the right wire. In addition,

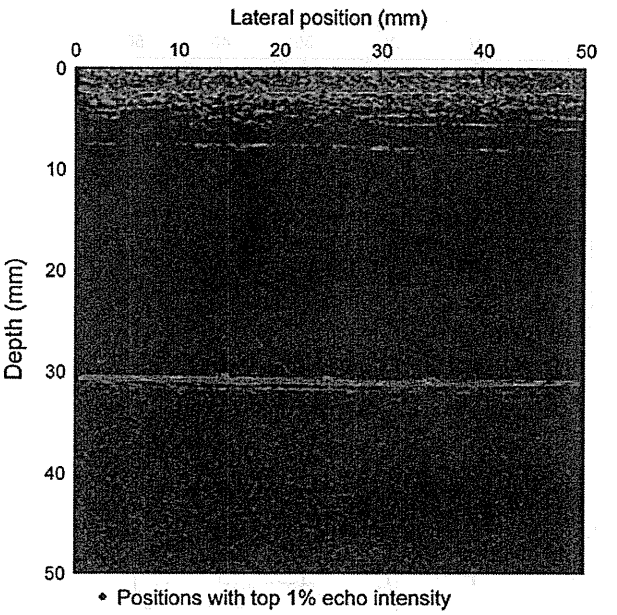

Fig. 8 Candidates for wire positions with high echo intensities. The intensity threshold was set to the top 1% intensity threshold

the strong suppression of the correlation coefficients appeared only behind the wire positions, indicating that the employment of a high correlation threshold can eliminate false images at the cost of the sensitivity of the method. When a correlation threshold parameter β of 3 was employed, i.e., the correlation threshold of $\mu - 3\sigma$ was employed, no false image appeared in this study. Therefore, a correlation threshold parameter β over 3 is useless under the conditions of this study.

Calcification depiction with a totalizing process

The degree of suppression in a correlation profile caused by a wire depends on the intensity threshold parameter α, as shown in Fig. 9. Therefore, we propose a calcification depiction method with a totalizing process. First, the method calculates three correlation profiles using three values for $\alpha = 0.05$, 0.1, and 0.2, where each profile uses a certain value for β. After the selection of calcification positions in the three correlation profiles, the method totals up all the selected positions and depicts them on the B-mode image.

When the method employs a small value for β, i.e., when a mild correlation threshold is employed, the sensitivity of the method improves at the cost of the appearance of false images. Since a correlation profile using a large value for α is less influenced by noise, a false image rarely appears in the profile. To improve the performance of the method, we employed a smaller value for β for the

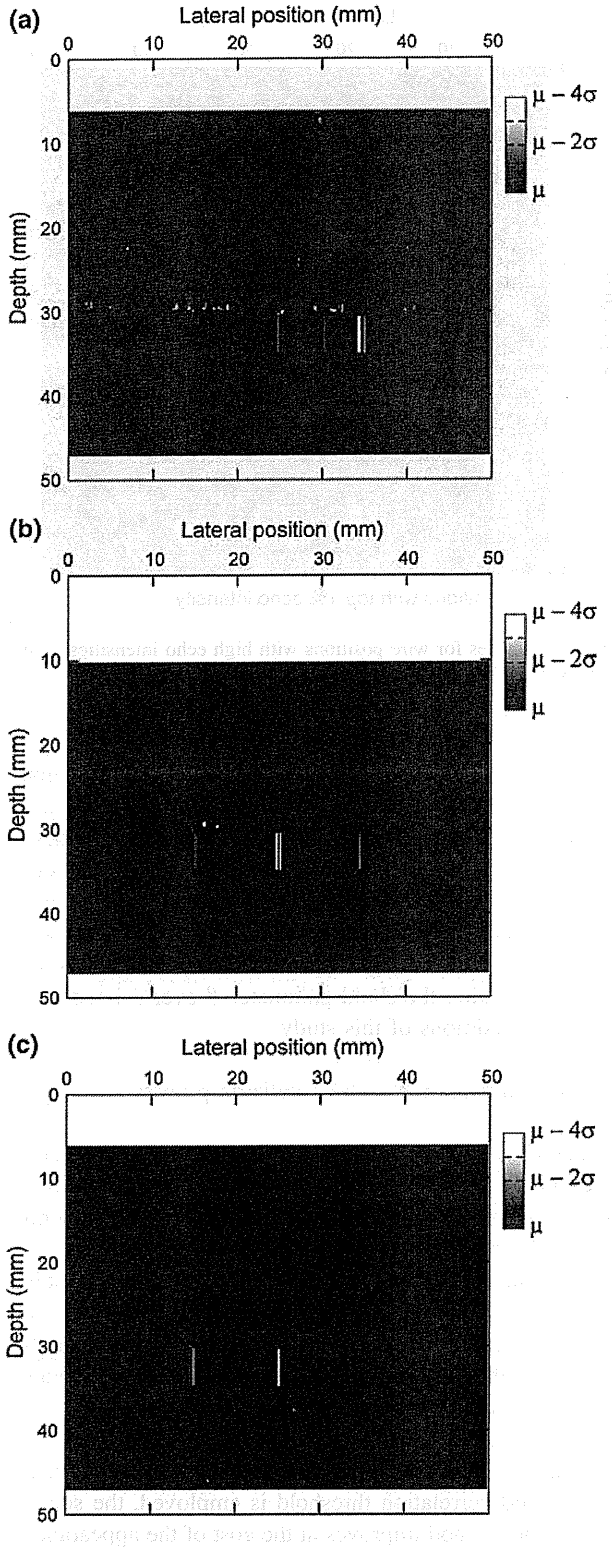

Fig. 9 Correlation profiles between adjacent scan lines employing three values of the intensity threshold parameter $\alpha =$ **a** 0.05, **b** 0.1, and **c** 0.2

Table 1 Threshold sets of three combinations of parameters α and β employed by the proposed calcification depiction method with a totalizing process

Threshold number	Combinations of parameters α and β
1	$(\alpha, \beta) = (0.05, 3), (0.1, 3), (0.2, 3)$
2	$(\alpha, \beta) = (0.05, 3), (0.1, 3), (0.2, 2)$
3	$(\alpha, \beta) = (0.05, 3), (0.1, 2), (0.2, 2)$
4	$(\alpha, \beta) = (0.05, 2), (0.1, 2), (0.2, 2)$

selection of calcification positions in a correlation profile with a larger value of α. As the employment of β over 3 is useless under the conditions of this study, we examined two cases, i.e., $\beta = 2$ and 3. Table 1 shows the four threshold sets utilized by the proposed calcification depiction method with a totalizing process, where a prior threshold number denotes a more severe threshold. As expected, employing a milder threshold yielded a higher sensitivity at the cost of the positive predictive value, as shown in Fig. 10. We calculated the sensitivity and the positive predictive value (PPV) of the method as N_D/N_T and $N_D/(N_D + N_{FP})$, respectively, where N_D, N_T, and N_{FP} are the number of detected wires, embedded wires, and false-positive wires, respectively. In this study, three wires were embedded in a phantom, i.e., $N_T = 3$. The sensitivity and PPV are presented as the mean ± standard deviation, where the number of samples is 5. The proposed calcification depiction method with the second threshold set depicted 11 of 15 wires embedded in five B-mode images of a phantom with a swine tissue layer, and all positions selected by the proposed method were located close to wires, as shown in Fig. 11, corresponding to a sensitivity of 73.3 ± 27.9% ($n = 5$) and a PPV of 100 ± 0% ($n = 5$). When PPV = 100%, the number of false-positive wires is 0; and thus the specificity also becomes 100%. This result suggests that the proposed calcification depiction has the potential to depict thin wires about 0.3 mm in diameter with both high sensitivity and good specificity.

Applied to a phantom without a swine tissue layer, the proposed methods with a totalizing process had high sensitivities with sufficient PPV. These results show that the proposed method has a high sensitivity and a good PPV for small calcification detection with sufficient robustness.

Conclusion

We propose a novel calcification depiction method that utilizes the decorrelation of forward scattered waves caused by the waveform change originating at a calcification

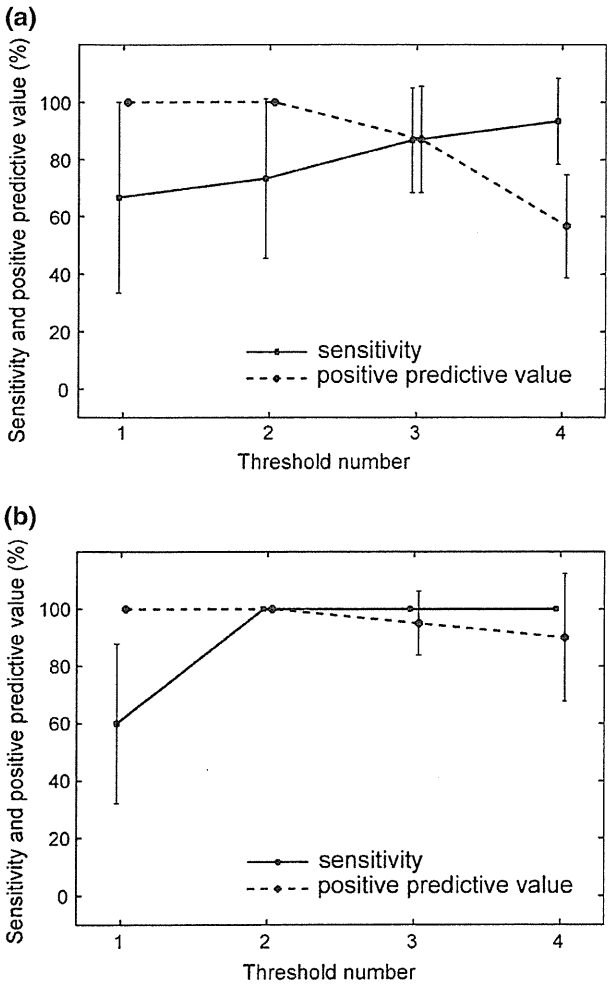

Fig. 10 Sensitivity and positive predictive value of the proposed calcification depiction method with a totalizing process for a calcification phantom **a** with and **b** without a swine cutaneous tissue layer

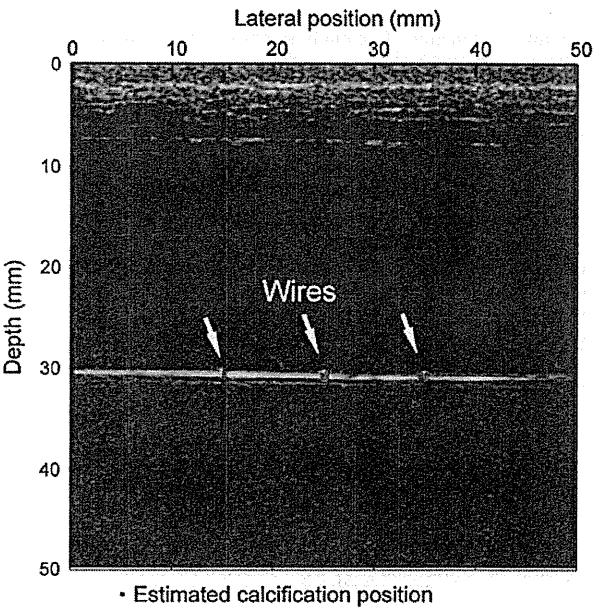

Fig. 11 Estimated wire positions in a calcification phantom with a swine tissue layer, where the proposed method with a totalizing process employed the second threshold set

location. A small calcification slightly changes the intensity of an ultrasound pulse causing no associated acoustic shadowing. However, it should change the waveform of the ultrasound pulse significantly. The proposed calcification depiction method depicted wires about 0.3 mm in diameter with a sensitivity of 73.3% and a specificity of 100%, where the wires might have gone undetected under clinical inspection of ultrasound B-mode images. This study suggests the probability that an US device will be able to perform calcification detection well. We investigated a situation where a single layered structure with calcifications exists in a homogeneous medium, simulating the calcifications in a gallbladder wall. Future work will examine a situation where calcifications and several layered structures exist in an inhomogeneous medium to investigate the potential for application of the proposed method to breast cancer screening.

Acknowledgments This work is partly supported by the Research and Development Committee Program of the Japan Society of Ultrasonics in Medicine and the Innovative Techno-Hub for Integrated Medical Bio-imaging Project of the Special Coordination Funds for Promoting Science and Technology from the Ministry of Education, Culture, Sports, Science and Technology (MEXT), Japan.

References

1. Özdemir H, Demir MK, Temizöz O, et al. Phase inversion harmonic imaging improves assessment of renal calculi: a comparison with fundamental gray-scale sonography. J Clin Ultrasound. 2008;36:16–9.
2. Fowler KAB, Locken JA, Duchesne JH, et al. US for detecting renal calculi with nonenhanced CT as a reference standard. Radiology. 2002;222:109–13.
3. Lamb PM, Perry NM, Vinnicombe SJ, et al. Correlation between ultrasound characteristics, mammographic findings and histological grade in patients with invasive ductal carcinoma of the breast. Clin Radiol. 2000;55:40–4.
4. Jacob D, Brombart JC, Muller C, et al. Analysis of the results of 137 subclinical breast lesions excisions. Value of ultrasonography in the early diagnosis of breast cancer. J Gynecol Obstet Biol Reprod (Paris). 1997;26:27–31.
5. Zhu Y, Weight JP. Ultrasonic nondestructive evaluation of highly scattering materials using adaptive filtering and detection. IEEE Trans Ultrason Ferroelect Freq Contr. 1994;41:26–33.
6. Kamiyama N, Okamura Y, Kakee A, et al. Investigation of ultrasound image processing to improve perceptibility of microcalcifications. J Med Ultrasonics. 2008;35:97–105.

7. Finn HM, Johnson RS. Adaptive detection mode with threshold control as a function of spatially sampled clutter-level estimates. RCA Rev. 1968;29:414–65.
8. Hansen VG, Ward HR. Detection performance of the cell averaging LOG/CFAR receiver. IEEE Trans Aerosp Electron Syst. 1972;5:648–52.
9. Schmidt T, Hohl C, Haage P, et al. Diagnostic accuracy of phase-inversion tissue harmonic imaging versus fundamental B-mode sonography in the evaluation of focal lesions of the kidney. AJR Am J Roentgenol. 2003;180:1639–47.
10. Rosenthal SJ, Jones PH, Wetzel LH. Phase inversion tissue harmonic sonographic imaging: a clinical utility study. AJR Am J Roentgenol. 2001;176:1393–8.
11. Szopinski KT, Pajk AM, Wysocki M, et al. Tissue harmonic imaging: utility in breast sonography. J Ultrasound Med. 2003;22:479–87.
12. Rosen EL, Soo MS. Tissue harmonic imaging sonography of breast lesions improved margin analysis, conspicuity, and image quality compared to conventional ultrasound. Clin Imaging. 2001;25:379–84.
13. Krücker JF, Meyer CR, LeCarpentier GL, et al. 3D spatial compounding of ultrasound imaging using image-based nonrigid registration. Ultrasound Med Biol. 2000;26:1475–88.
14. Moskalik A, Carson PL, Meyer CR, et al. Registration of 3-dimensional compound ultrasound scans of the breast for refraction and motion correction. Ultrasound Med Biol. 1995; 21:769–78.
15. Rohling RN, Gee AH, Berman L. Automatic registration of 3-D ultrasound images. Ultrasound Med Biol. 1998;24:841–54.
16. Huber S, Wagner M, Medl M, et al. Real time spatial compound imaging in breast ultrasound. Ultrasound Med Biol. 2002;28: 155–63.
17. Weinstein SP, Conant EF, Sehgal C. Technical advances in breast ultrasound imaging. Semin Ultrasound CT MR. 2006;27:273–83.
18. Taki H, Sakamoto T, Yamakawa M, et al. Calculus detection for medical acoustic imaging using cross-correlation: simulation study. J Med Ultrasonics. 2010;37:129–35.
19. Taki H, Sakamoto T, Yamakawa M, et al. Small calculus detection for medical acoustic imaging using cross-correlation between echo signals. Proc IEEE Int Ultrason Symp. 2009; 2398–2401.

Comparison of Uterine Peristalsis Before and After Uterine Artery Embolization at 3-T MRI

Aki Kido[1]
Susan M. Ascher[2]
Keiko Kishimoto[3]
Winnie Hahn[4]
Reena C. Jha[2]
Kaori Togashi[1]
James B. Spies[2]

OBJECTIVE. The purpose of this article is to compare uterine peristalsis before and after uterine artery embolization (UAE) on a 3-T MRI system.

SUBJECTS AND METHODS. MRI scans were prospectively performed for 20 women with symptomatic uterine fibroids (age range, 39–53 years) before and after UAE in the periovulatory phase with a 3-T scanner. Sagittal T2 turbo spin-echo sequences and a HASTE sequence were obtained. Sixty HASTE images were obtained for 3 minutes to display on cine mode. Two radiologists independently evaluated the datasets for the presence of uterine peristalsis using a 5-point rating scale. When peristalsis was present, the direction and frequency were recorded. The images were also evaluated for index fibroid location before and after UAE, index fibroid volume, uterine volume, and fibroid burden estimate.

RESULTS. The presence and frequency of uterine peristalsis increased after UAE for both readers, but was significant only for the presence of uterine peristalsis. The majority of patients had peristalsis in the cervix-to-fundus direction. In six cases, uterine peristalsis emerged after UAE. Uterine volumes before UAE were significantly smaller in these six cases compared with the remaining 14 cases, though no significant difference was found in the reduction rate of the uterus or fibroid volumes. The index fibroid was intramural in three of the six cases with interval appearance of peristalsis. The fibroid was solitary in four of the six cases.

CONCLUSION. Cine MRI at 3 T may show recovery of uterine peristalsis in some women with symptomatic fibroids after successful UAE.

Keywords: 3-T MRI, uterine artery embolization, uterine peristalsis

DOI:10.2214/AJR.10.5349

Received July 16, 2010; accepted after revision October 27, 2010.

[1]Department of Diagnostic Radiology and Nuclear Medicine, Kyoto University, 57 Shogoin Kawaharacho, Sakyo-ku, Kyoto City, Kyoto, Japan 6068507. Address correspondence to A. Kido (akikido@kuhp.kyoto-u.ac.jp).

[2]Department of Radiology, Georgetown University Hospital, Washington, DC.

[3]Present address: St. Marianna University School of Medicine, Toyoko Hospital, Kawasaki City, Kanagawa, Japan.

[4]Present address: Mid Atlantic Permanente Medical Group, Rockville, MD.

AJR 2011; 196:1431–1435

0361–803X/11/1966–1431

Uterine leiomyomas or fibroids are the most common benign tumors of the uterus and are present in at least 20% of women of reproductive age [1]. Approximately half of women with fibroids experience symptoms [1]. Transcatheter uterine artery embolization (UAE) has emerged as a minimally invasive, safe, and effective treatment option for patients with symptomatic uterine fibroids. The long-term outcome for women undergoing UAE is comparable to that for myomectomy and hysterectomy [2–5].

Uterine peristalsis is a subtle and rhythmic contraction of the subendometrial myometrium that aids in sperm transport and menstrual blood egress. Fibroids may suppress or disrupt normal rhythmic contractile waves [6, 7]. Transvaginal ultrasound was originally performed for evaluating uterine peristalsis; however, T2-weighted MRI, especially cine MRI, improves the conspicuity for detecting subtle movement less invasively [8–10]. Several studies have shown the utility of 3-T systems for evaluating the female pelvis [11, 12]. In fact, Kataoka et al. [12] found that 3-T HASTE, the sequence used to evaluate peristalsis, was superior to 1.5-T HASTE for the following parameters: overall image quality, endometrial–junctional zone contrast, and myometrium–junctional zone contrast. Therefore, the increasing availability of high-field MRI may offer the potential for improved identification and characterization of uterine peristalsis [11, 12].

The goal of our study was to test our hypothesis that absent or disorganized uterine peristalsis caused by fibroids would be improved after successful UAE with reduction in fibroid volume and that this improvement could be evaluated using 3-T MRI.

Subjects and Methods

Study Population

The protocol of this prospective study was approved by the institutional review board of our institution. Written informed consent was obtained from all the participants.

During a 14-month period, we recruited 23 women with symptomatic uterine fibroids undergoing evaluation for UAE to participate in our study. Patients who were menopausal or taking hormone replacement therapy (n = 1, after UAE) were excluded from the study because of previous reports indicating that these two conditions have adverse effects on peristalsis [13, 14]. Patients were also excluded if their endometrium was not well seen (n = 1, at follow-up MRI) because of the difficulty in evaluating uterine peristalsis in this circumstance. An additional patient was excluded because UAE was canceled (n = 1). Therefore, of the 23 patients initially included in our study, three were subsequently excluded and 20 patients (age range, 39–53 years; mean age, 45.5 ± 3.7 years) compose our study group.

MRI Scanning Protocol

MRI studies were performed before and after UAE on both a 1.5-T system (Symphony, Siemens Healthcare) and a 3-T research system (Magnetom Trio, Siemens Healthcare) with an eight-channel body phased-array coil. The 1.5-T examination was performed as a standard fibroid evaluation, whereas the research 3-T examination was performed solely for uterine peristalsis evaluation.

The interval between MRI examination and UAE was 28.5 ± 25.3 days (range, 3–83 days), and the interval between UAE and follow-up imaging was 103 ± 24.5 days (range, 63–159 days) after UAE. MRI scans were performed during the late follicular to early luteal phase. This period was chosen because uterine peristalsis is reported to increase during the follicular phase and is most conspicuous during the periovulatory phase [8, 9, 15]. The date of ovulation was defined as 14 days before the anticipated start of the next menstrual cycle. MRI scans were performed within 5 days before or after the expected date of ovulation.

We performed our standard before- and after-UAE protocol in all patients at 1.5 T and then moved the patient to the 3-T research system for the cine peristalsis evaluation. Our standard 1.5-T protocol includes an axial image of the pelvis; sagittal, axial, and coronal images of the uterus using the HASTE sequence; sagittal T1- and T2-weighted turbo spin-echo sequences; and sagittal dynamic fat-suppressed volumetric interpolated breath-hold examination images acquired before and at 30, 60, and 90 seconds after IV injection of gadopentate dimeglumine (Magnevist, Berlex Laboratories) at a dose of 0.1 mmol/kg of body weight. To evaluate uterine peristalsis, we also acquired 60 serial HASTE images obtained during quiet respiration over 3 minutes in the midsagittal plane of the uterus. No premedication was given to subjects before examination. Experienced angiographers performed UAE according to a previously described technique that includes bilateral selective UAE using either 355–500 μm polyvinyl alcohol particles (Contour, Boston Scientific) or 500–700 μm tris-acryl gelatin microspheres (Embosphere Microspheres, Biosphere Medical) [16].

TABLE 1: Presence of Uterine Peristalsis for Readers A and B Before and After Uterine Artery Embolization (UAE)

Finding	Before UAE		After UAE	
	Reader A	Reader B	Reader A	Reader B
Uterine peristalsis present (no. of cases)	4[a]	2[b]	7[a]	7[b]
Direction of peristalsis (no. of cases)				
Cervix to fundus	3	2	3	7
Fundus to cervix	0	0	0	0
Disorganized	1	0	4	0
Frequency (no. of waves)[c]	1.3	2.5	4.5	4.0

[a] $p < 0.01$ for the difference between peristaltic presence before and after UAE for reader A.
[b] $p < 0.05$ for the difference between peristaltic presence before and after UAE for reader B.
[c] $p > 0.05$ for the difference between peristaltic frequency before and after UAE for both readers A and B.

Image Analysis

Cine MRI was constructed from 60 serial 3-T HASTE images using a commercially available software program (Ulead Media Studio Pro. 6.0, Corel Japan). Two radiologists independently evaluated cine MRI scans for the presence or absence of peristalsis. Reader A, with 9 years of general female pelvic MRI experience, had 3 months of experience evaluating uterine peristalsis; reader B, with 11 years of general female pelvic MRI experience, had 5 years of experience evaluating uterine peristalsis. Uterine peristalsis was defined as "present" if the endometrium changed in configuration during the cine sequence, or if the low-signal-intensity junctional zone changed configuration during the cine sequence. The presence of uterine peristalsis was rated on a scale of 1 to 5, with 5 defined as definitely present, 4 defined as probably present, 3 defined as cannot determine whether present or

TABLE 2: Presence of Uterine Peristalsis Before and After Uterine Artery Embolization (UAE) for Each Case for Readers A and B

Case No.	Before UAE		After UAE	
	Reader A	Reader B	Reader A	Reader B
1	Absent	Absent	Absent	Absent
2	Absent	Absent	Absent	Absent
3	Absent	Absent	Emergent	Emergent
4	Absent	Absent	Emergent	Emergent
5	Absent	Absent	Absent	Absent
6	Present	Present	Present	Present
7	Present	Absent	Absent	Absent
8	Present	Present	Absent	Absent
9	Absent	Absent	Absent	Absent
10	Absent	Absent	Emergent	Emergent
11	Absent	Absent	Emergent	Emergent
12	Absent	Absent	Absent	Absent
13	Absent	Absent	Absent	Absent
14	Absent	Absent	Absent	Absent
15	Absent	Absent	Absent	Absent
16	Present	Absent	Absent	Absent
17	Absent	Absent	Emergent	Emergent
18	Absent	Absent	Absent	Absent
19	Absent	Absent	Emergent	Emergent
20	Absent	Absent	Absent	Absent

absent, 2 defined as probably not present, and 1 defined as definitely not present. For the purpose of analysis, peristalsis was scored as present for cases rated 4 or 5. Peristalsis was scored as absent for cases rated 1, 2, or 3.

When peristalsis was present, the radiologists also evaluated the images for peristalsis direction and frequency. Direction of peristalsis was categorized as cervix-to-fundus, fundus-to-cervix, and disorganized (both cervix-to-fundus and fundus-to-cervix during the cine MRI). Peristalsis frequency was recorded as the number of peristalsis waves per 3-minute interval.

The volume of the uterus and that of the largest fibroid (i.e., the index fibroid) were measured on sagittal T2-weighted images by radiologist B using a prolate ellipse: volume (cm^3) = length × width × height × 0.523. The reduction in uterine and fibroid volume were calculated and expressed as a percentage, as follows: 100 × (volume before UAE – volume after UAE) / volume before UAE, according to a previous report [17].

The location of the index fibroid was classified into four groups by radiologist B as follows: intramural, submucosal, intracavitary, or subserosal fibroids. For the purpose of this study, if a fibroid spanned two locations (e.g., intramural and submucosal), its majority component determined its location.

The number of the fibroids was counted using all sagittal T2-weighted images by one radiologist. Fibroid burden was categorized as 1, 2–5, 6–10, or more than 10.

Statistical Analysis

Interobserver agreement of two readers for the presence of uterine peristalsis was evaluated with kappa coefficient. The level of agreement was defined as follows: kappa values of 0–0.20, poor; kappa values of 0.21–0.40, fair; kappa values of 0.41–0.60, moderate; kappa values of 0.61–0.80, good; and kappa values of 0.81–0.99, excellent [18].

A change in the presence of peristalsis before and after UAE was compared by Pearson's chi-square test. Changes in uterine and index fibroid volume, uterine and index fibroid reduction rates, and the frequency of peristalsis before and after UAE were compared by use of an unpaired Student *t* test. Analysis was done using SPSS software (version 11, SPSS).

TABLE 3: Volume of Uterus and Index Fibroids, Location of Index Fibroid, and Number of Fibroids Before and After Uterine Artery Embolization (UAE) in All 20 Cases

Parameter	Before UAE	After UAE
Volume (mL), mean ± SD[a]		
Uterus	535.1 ± 236.7	362.4 ± 183.8
Index fibroid	95.4 ± 68.4	53.3 ± 46.7
Location of index fibroid (no. of cases)		
Intramural	8	9
Submucosal	10	6
Intracavitary	1	4
Subserosal	1	1
No. of fibroids/case (no. of cases)		
1	6	7
2–5	6	9
6–10	5	3
>10	3	1

[a] $p < 0.05$ for both uterine and index fibroid volume before and after UAE.

Results

UAE was technically successful in all patients; both uterine arteries were embolized, and there were no associated adverse events after UAE. Results for the presence of uterine peristalsis are shown in Tables 1 and 2. For both readers, the presence of uterine peristalsis increased after UAE. For reader A, uterine peristalsis was present in four of 20 patients before UAE and in seven of 20 patients after UAE. Specifically, uterine peristalsis was unchanged in one case, emerged in six cases, and disappeared in three cases. For reader B, uterine peristalsis was present before UAE in two of 20 patients and in seven of 20 patients after UAE. Specifically, uterine peristalsis was unchanged in one case, emerged in six cases, and disappeared in one case. The six cases of newly emerged peristalsis were the same cases for both readers (Table 2). Interobserver agreement for the two readers for the presence of uterine peristalsis before and after UAE was 0.77 and 0.89, respectively, meaning that the agreement between the two readers was good to excellent. For both readers, the increase in the presence of uterine peristalsis after UAE was significant (reader A, $p < 0.01$; reader B, $p < 0.05$). The frequency of uterine peristalsis also increased after UAE for both readers, though the increase was not significant ($p > 0.05$). In the majority of cases, the direction of uterine peristalsis was cervix-to-fundus both before and after UAE.

TABLE 4: Comparison Between Six Cases Where Peristalsis Newly Emerged After Uterine Artery Embolization (UAE) and Remaining 14 Cases

			Volume (mL)				Volume Reduction Rate (%)		Location of Index Fibroid (No. of Cases)				No. of Fibroids/ Case (No. of Cases)			
			Uterus		Index Fibroid											
Uterine Peristalsis	No. of Cases	Age (y), Mean	Before UAE	After UAE	Before UAE	After UAE	Uterus	Index Fibroid	Intramural	Submucosal	Intracavitary	Subserosal	1	2–5	6–10	>10
No change or not present	14	44.7	609.95	395.51	106.5	59.91	35.2	43.7	5	8	1	0	2	5	4	3
Newly emerged	6	47.3	360.52	273.63	69.54	34.75	24.1	50.0	3	2	0	1	4	1	1	0
p	—	0.15	<0.05	0.19	0.28	0.29	0.86	0.52	—	—	—	—	—	—	—	—

Note—Dashes indicate that *p* value was not calculated.

Table 3 displays the results for the volume of the uterus and index fibroids, location of the index fibroid, and the number of the fibroids both before and after UAE. The volume of both the uterus and index fibroid was significantly reduced after UAE compared with before UAE ($p < 0.05$).

Table 4 displays results for the six cases of newly emerged peristalsis after UAE compared with the remaining 14 cases to include uterine and index fibroid volume and reduction rate, index fibroid location, and fibroid burden before UAE.

The only significant difference between these two groups was the uterine volume before UAE. Uterine volume before UAE in patients where peristalsis newly emerged was 360.52 mL, whereas it was 609.95 mL in patients without a change in peristalsis or with interval disappearance of peristalsis.

Table 5 displays the reduction rate of the index fibroids grouped according to fibroid location (before UAE). Most of the index fibroids were intramural or submucosal in location and had reduction rates of 39% and 53%, respectively.

TABLE 5: Reduction Rate of Index Fibroid Compared by Classification of Fibroid Location Before Uterine Artery Embolization

Location of Index Fibroid	Reduction Rate (%)	No. of Cases
Intramural	39	8
Submucosal	53	10
Intracavitary	86	1
Subserosal	52	1

Discussion

Our study found that uterine peristalsis was present in more patients after UAE than before UAE. Two readers with varying experience both identified uterine peristalsis at a significantly greater frequency after UAE. Agreement between the two readers was good to excellent. Although the exact mechanism of fibroids on uterine peristalsis has not been well established, it is possible that some fibroids, by either mechanical or functional means, may suppress or disrupt the normal peristaltic wave propagation of the inner myometrium [9, 10]. That uterine peristalsis emerged or normalized after successful UAE suggests that a decrease in fibroid or uterine volume may allow recovery of uterine muscle function. Additionally, there was a trend toward increased peristaltic frequency after successful UAE, although this was not significant.

As for peristaltic direction, most of the cases showed cervix-to-fundus waves in the periovulatory phase. This is in accordance with previously published reports [8, 9, 15]. In our study, reader A noted four cases of disorganized direction on 3-T cine before UAE. Reader B, who had more experience, was able to determine peristalsis direction in all cases. This may reflect reader A's relative inexperience in evaluating uterine peristalsis.

In six of 20 cases, uterine peristalsis was newly recognized after successful UAE. In these six cases, uterine volume was significantly smaller before UAE than in the remaining 14 cases. Additionally, the index fibroid reduction rate in these cases with emergent peristalsis was larger than the remaining cases, although the difference was not significant. These results parallel those of a previous report whereby the fibroid volume reduction rate after UAE was greatest in the cases with smaller pre-UAE uterine volumes [17]. The same trend may apply to uterine peristalsis—uterine peristalsis may recover in a smaller baseline (pre-UAE) uterus that undergoes successful UAE. Perhaps there is a threshold uterine volume below which uterine peristalsis may recover. Consequently, a smaller baseline uterine volume coupled with post-UAE decrease in index fibroid volume may cross the threshold that allows restoration of normal peristalsis. More work needs to be done to evaluate this phenomenon.

Of the six patients with emergent peristalsis, the index fibroid location was intramural in three patients, submucosal in two patients, and subserosal in one patient (Fig. 1; Figures S1 and S2 can be seen in the *AJR* electronic supplement to this article, available at www.ajronline.org, and present more detail than the figures printed here). Nishino et al. [6] and Orisaka et al. [7] reported that submucosal fibroids disturbed uterine contractions. Our study suggests that, in addition to submucosal fibroids, other

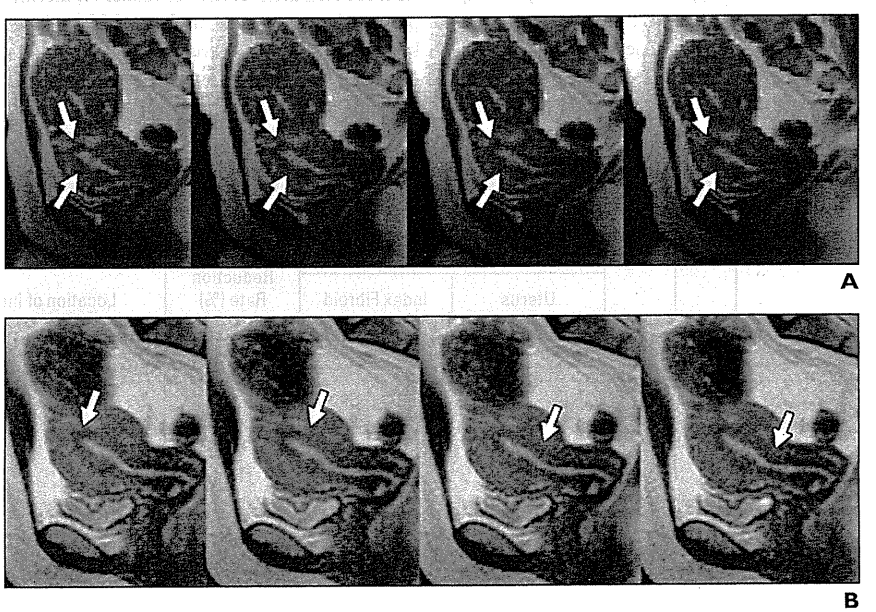

Fig. 1—Uterine peristalsis recovery in 41-year-old woman with subserosal and intramural leiomyomas, before and after uterine artery embolization (UAE).
A, Four serial images were selected from 60 serial HASTE images obtained before UAE (TR/TE, 3000/90; slice thickness, 5 mm; flip angle, 150°; bandwidth, 698 Hz; voxel size, 1.0 × 1.0 × 5.0 mm). Junctional zone (*arrows*) in fundus and anterior corpus does not change in thickness, nor does signal intensity over course of series.
B, Four serial HASTE images obtained after UAE show interval appearance of uterine peristalsis. Lowest signal intensity region within posterior junctional zone (*arrows*) moves from cervix to fundus accompanied with change of endometrial configuration. Anterior corpus did not change.
See also Figure S1, uterine peristalsis recovery, and Figure S2, no uterine peristalsis recovery, in supplemental data online.

fibroid locations may disturb uterine contraction. This warrants detailed study with more cases. Although our results for fibroid reduction rates do parallel those of Jha et al. [17], with submucosal fibroids showing the most marked volume reduction 3 months after UAE, this marked decrease did not consistently translate to peristalsis recovery. The presence of submucosal fibroids itself may be sufficient to disturb uterine peristalsis, regardless of the size of fibroids; therefore, peristalsis recovery is not ensured with index submucosal fibroid reduction. Perhaps the decrease in index intramural fibroid volume has more of an effect on uterine contractility because uterine peristalsis is a function of myometrial smooth muscle and not the endometrium.

Concerning fibroid burden and peristalsis recovery, four of six cases of emergent peristalsis after UAE were in patients with a solitary fibroid. Fibroids are well known to deform uterine shape and distort the endometrium. However, a uterus with a single fibroid may not have the same amount of deformation and distortion as a uterus with multiple fibroids. After successful UAE, volume reduction of a solitary fibroid may be more apt to restore uterine and endometrial shape and be associated with a better rate of uterine peristalsis emergence.

That uterine peristalsis normalized or emerged after successful UAE may affect fertility. Specifically, normal cervix-to-fundus contractions may lead to more efficient sperm transport and, thus, increased fertilization rates, whereas loss of disorganized contractions may aid implantation. Clearly, this is an exciting area for further study.

Our study has several limitations. First, the follow-up interval after UAE was only 3 months. Although Jha et al. showed an almost 40% reduction rate in the uterine volume at 3 months after UAE, they showed an almost 60% reduction 1 year after UAE [17]. That is, we may have underestimated uterine peristalsis normalization; long-term follow-up might have shown further uterine peristalsis recovery. Second, we imaged patients on a 3-T system. Although 3 T has been shown to increase uterine peristalsis conspicuity [12], the high field strength may have also introduced unforeseen confounding movements, such as subtle changes in organ position during respiration. Third, the evaluation was done by two readers with differing experience in evaluating uterine peristalsis. That there was good-to-excellent agreement between the two readers suggests that this is a relative limitation. Fourth, because patients with symptomatic fibroids often have irregular menses, it is possible that we may not have imaged during peak peristalsis.

In conclusion, our study shows an increase in the presence of uterine peristalsis after successful UAE, and this increase is demonstrable on 3-T cine MRI.

Acknowledgments

We thank John VanMeter for technical assistance, Hillary Mead and Fatemah Kianpour for their dedicated assistance in facilitating patient scheduling, and Ashley Stowell for manuscript assistance.

References

1. Hillard PJA. Benign diseases of the female reproductive tract: symptoms and signs. In: Berek J, ed. *Novak's gynecology*, 13th ed. Philadelphia, PA: Lippincott Williams & Wilkins, 2002:351–420
2. Spies JB, Cooper JM, Worthington-Kirsch R, Lipman JC, Mills BB, Benenati JF. Outcome of uterine embolization and hysterectomy for leiomyomas: results of a multicenter study. *Am J Obstet Gynecol* 2004; 191:22–31
3. Spies JB, Bruno J, Czeyda-Pommersheim F, Magee ST, Ascher SA, Jha RC. Long-term outcome of uterine artery embolization of leiomyomata. *Obstet Gynecol* 2005; 106:933–939
4. Pron G, Bennett J, Common A, Wall J, Asch M, Sniderman K. The Ontario Uterine Fibroid Embolization Trial. Part 2. Uterine fibroid reduction and symptom relief after uterine artery embolization for fibroids. *Fertil Steril* 2003; 79:120–127
5. Mara M, Fucikova Z, Maskova J, Kuzel D, Haakova L. Uterine fibroid embolization versus myomectomy in women wishing to preserve fertility: preliminary results of a randomized controlled trial. *Eur J Obstet Gynecol Reprod Biol* 2006; 126:226–233
6. Nishino M, Togashi K, Nakai A, et al. Uterine contractions evaluated on cine MR imaging in patients with uterine leiomyomas. *Eur J Radiol* 2005; 53: 142–146
7. Orisaka M, Kurokawa T, Shukunami K, et al. A comparison of uterine peristalsis in women with normal uteri and uterine leiomyoma by cine magnetic resonance imaging. *Eur J Obstet Gynecol Reprod Biol* 2007; 135:111–115
8. Lyons EA, Taylor PJ, Zheng XH, Ballard G, Levi CS, Kredentser JV. Characterization of subendometrial myometrial contractions throughout the menstrual cycle in normal fertile women. *Fertil Steril* 1991; 55:771–774
9. Kunz G, Beil D, Deininger H, Wildt L, Leyendecker G. The dynamics of rapid sperm transport through the female genital tract: evidence from vaginal sonography of uterine peristalsis and hysterosalpingoscintigraphy. *Hum Reprod* 1996; 11: 627–632
10. Nakai A, Togashi K, Kosaka K, et al. Uterine peristalsis: comparison of transvaginal ultrasound and two different sequences of cine MR imaging. *J Magn Reson Imaging* 2004; 20:463–469
11. Hori M, Kim T, Murakami T, et al. Uterine cervical carcinoma: preoperative staging with 3.0-T MR imaging: comparison with 1.5-T MR imaging. *Radiology* 2009; 251:96–104
12. Kataoka M, Kido A, Koyama T, et al. MRI of the female pelvis at 3T compared to 1.5T: evaluation on high-resolution T2-weighted and HASTE images. *J Magn Reson Imaging* 2007; 25:527–534
13. Maslow KD, Lyons EA. Effect of oral contraceptives and intrauterine devices on midcycle myometrial contractions. *Fertil Steril* 2003; 80:1224–1227
14. Kido A, Togashi K, Nakai A, Kataoka ML, Koyama T, Fujii S. Oral contraceptives and uterine peristalsis: evaluation with MRI. *J Magn Reson Imaging* 2005; 22:265–270
15. Nakai A, Togashi K, Yamaoka T, et al. Uterine peristalsis shown on cine MR imaging using ultrafast sequence. *J Magn Reson Imaging* 2003; 18: 726–733
16. Spies JB, Allison S, Flick P, et al. Spherical polyvinyl alcohol versus tris-acryl gelatin microspheres for uterine artery embolization for leiomyomas: results of a limited randomized comparative study. *J Vasc Interv Radiol* 2005; 16:1431–1437
17. Jha RC, Ascher SM, Imaoka I, Spies JB. Symptomatic fibroleiomyomata: MR imaging of the uterus before and after uterine arterial embolization. *Radiology* 2000; 217:228–235
18. Landis JR, Koch GG. The measurement of observer agreement for categorical data. *Biometrics* 1977; 33:159–174

FOR YOUR INFORMATION

A data supplement for this article can be viewed in the online version of the article at: www.ajronline.org.

Clinical Radiology 66 (2011) 1060–1063

Contents lists available at ScienceDirect

Clinical Radiology

journal homepage: www.elsevierhealth.com/journals/crad

Original Paper

Whole-heart coronary MR angiography under a single breath-hold: A comparative study with respiratory-gated acquisition using a multi-element phased-array coil

T. Okada [a,*], S. Kanao [a], S. Kuhara [b], A. Ninomiya [b], K. Fujimoto [a], A. Kido [a], K. Togashi [a]

[a] *Diagnostic Imaging and Nuclear Medicine, Kyoto University Graduate School of Medicine, Sakyoku, Kyoto, Japan*
[b] *Toshiba Medical Systems Corporation, Otawara-shi, Tochigi, Japan*

ARTICLE INFORMATION

Article history:
Received 3 April 2011
Received in revised form
31 May 2011
Accepted 6 June 2011

AIM: To compare visualization using whole-heart coronary magnetic resonance angiography (CMRA) acquired during a single breath-hold (BH) with that using conventional respiratory-gated (RG) CMRA.

MATERIALS AND METHODS: The CMRAs of 14 healthy subjects under either BH or RG conditions were studied using a 1.5 T system equipped with a whole-body phased-array coil and 16-channel receivers. The BH examination was accelerated using parallel imaging (PI) by factors of 2.5 and 2 in the phase and section directions, respectively. For the RG examination, a PI factor of 2 was used only in the phase direction. The visualization quality of 15 coronary segments using each condition was evaluated with a five-point scale (0–4). Differences between two conditions were compared at segments with an average score greater than 2 in RG-CMRA.

RESULTS: The average examination time for BH and RG acquisition scans was 34 s and 11 min 31 s, respectively. Ten segments (segments 1–3, 5–9, 11, and 13) had average scores higher than 2 in RG-CMRA. Of these, BH-CMRA had significantly lower scores than RG-CMRA at six segments (segments 1, 5–8, and 11) after correction for multiple comparisons ($p < 0.005$). However, in BH-CMRA, proximal segments (segments 1–2, 5–7, and 11) showed average scores over 2, indicating marginally acceptable image quality.

CONCLUSION: Compared with the relatively limited degree of image degradation with RG-CMRA, the present data suggest that BH-CMRA would be useful for screening and as an adjunct to RG-CMRA that is occasionally incomplete.

Introduction

Coronary magnetic resonance angiography (CMRA) is usually acquired under respiratory gating (RG) with compensation of displacement of the heart.[1,2] CMRA is initially conducted in a volume-targeted approach. However, the need for accurate localization of the coronary arteries makes the technique operator-dependent, and only limited regions can be evaluated. Hence, a whole-heart approach has been suggested.[3,4] The images using this approach were reported to show good agreement with reference images taken using conventional angiography, although the scan times are frequently as long as 14 min[5] due to the inevitable rejection of acquired data,[6] the effect of respiratory motion,[7,8] and changes in breathing pattern.[8,9] The long scan time also makes RG-CMRA prone to image artefacts caused by arrhythmia and body motion.[10,11]

* Guarantor and correspondent: T. Okada, Department of Diagnostic Radiology, Kyoto University, 54 Shogoin Kawaharacho, Sakyoku, Kyoto 606-8507, Japan. Tel.: +81 75 751 4215; fax: +81 75 751 4216.
E-mail address: tomokada@kuhp.kyoto-u.ac.jp (T. Okada).

0009-9260/$ – see front matter
doi:10.1016/j.crad.2011.06.004

To overcome these problems, scan acceleration has been attained using the parallel imaging (PI) method[12] that employs multiple phased-array coils. Acceleration with PI is typically performed in one dimension, although the development of phased-array coils consisting of multiple coil elements that cover wide body areas has enabled two-dimensional (2D) PI.[13–15] A 32-channel coil system dedicated to the heart has enabled whole-heart CMRA within a single breath-hold (BH).[16] BH-CMRA facilitates a wider usage of MR for the examination of coronary artery disorders without radiation exposure and administration of contrast material, which may contribute to improved public healthcare. However, the availability of dedicated cardiac coil systems is limited. Nevertheless, multi-array body coil systems consisting of more than 10 coils for wide body coverage are increasingly becoming clinically available, allowing PI in two dimensions.

In the present study, it was hypothesized that a multi-array coil system would increase the speed of coronary imaging. Therefore, the capability of a multi-array body coil system for BH-CMRA as a reference with maximum use of PI was investigated.

Materials and methods

Subjects

This study was approved by the Institutional Committee on Human Research. Fourteen healthy volunteers (10 men and four women; mean age 24 years, range 20–42 years) without previous history of disease were enrolled in this study, after obtaining written informed consent.

Imaging protocol

The examinations were conducted using a 1.5 T MR system (Vantage powered by Atlas; Toshiba Medical Systems Corporation, Otawara-shi, Japan) equipped with a pair of body array coils, each of which consisted of 4×4 arrays. The arrays were placed at both the front and back of the chest. Two top rows were used for both the front and back coils to cover the entire heart, resulting in 16 active coil elements connected to 16 receiver channels.

Localizing images were acquired for the heart and the diaphragm in three orthogonal stacks, followed by a reference scan to determine the individual coil sensitivities for subsequent PI. Cine images were scanned in four-chamber view using a balanced steady-state free precession (bSSFP) sequence for 50–60 frames per heart beat with the following parameters: 4.3 ms repetition time (TR), 2.2 ms echo time (TE), and 120° flip angle (FA). By reviewing these images, the interval of minimal right coronary artery (RCA) motion was visually assessed, and acquisition windows for all subsequent scans were planned to fall within a period of minimal RCA motion.[3] Respiratory motion during the acquisition of the coronary scans was compensated for using prospective real-time gating (gating window width 4.65 mm) and volume tracking with a motion correction factor of 0.6, based on the one-dimensional (1D) data of the right diaphragm position.[17] For cardiac synchronization and monitoring, two electrodes were placed on the left anterior hemithorax of the subject and the R wave of the electrocardiogram was used as a trigger for image acquisition.

Whole-heart coronary images were acquired in two conditions of BH and RG with adaptive correction of the diaphragm motion using a three-dimensional (3D), centric-ordered, segmented, bSSFP sequence (4.3 ms TR, 2.2 ms TE, and 120°FA) to cover the entire heart in 70–80 transverse sections of 1.5 or 2.5 mm thickness for RG and BH imaging, respectively. In-plane resolutions were 1.3×1.5 to 2.2×2.5 mm for BH and 1.3×1.5 to 1.9×1.5 mm for RG. For BH-CMRA, 2D PI was applied in the phase direction by a factor of 2.5 and in the section direction by a factor of 2. For RG-CMRA, 1D PI was used in the phase direction by a factor of 2. The length of the acquisition window for each rest period was 279.3 ms (one segment) and 98.7 ms (four segments) for BH and RG scans, respectively. The image was reconstructed to the voxel size of $0.6 \times 0.6 \times 0.75$ mm^3 in both cases.

Image processing and quality assessment

The 3D CMRA data were transferred to a commercially available workstation with image reconstruction software (AZE Virtual Place; AZE, Tokyo, Japan). For each of the RCA, the left anterior descending (LAD) and left circumflex (LCX) multiple contiguous sections were selected, and a curved planar reconstruction (CPR) was conducted by a radiological technologist. Radiologists were blinded to the order of subject data processing during evaluation.

Assessment of 3D CMRA was conducted segment-wise as classified by the American Heart Association: the RCA was divided into segments 1–4, the LAD was divided into segments 5–10, and the LCX was divided into segments 11–15 by two readers (T.O., S.K.) in consensus. In order to grade the image quality of all the coronary artery segments, a five-point grading system was used: 4, excellent (the vessel was well depicted with sharply defined borders); 3, fair (the vessel was adequately visualized, with confidence in the diagnosis, only mildly blurred borders); 2, good (coronary was visible, but confidence in the diagnosis was low due to moderately blurred borders); 1, poor (coronary vessel barely seen or was obscured by noise); and 0, not visualized.[5,18] For the evaluation, both the original and CPR images were used. Differences in scores between BH-CMRA and RG-CMRA were compared by the Wilcoxon signed rank test. Statistical comparisons were conducted in the segments where average scores were higher than 2 in RG-CMRA (reference standard). A p-value less than 0.05 was considered statistically significant after Bonferroni correction for multiple comparisons.

Results

The average heart rate of the subjects was 57.4 beats/min (range 46–69 beats/min), and the acquisition was performed at the cardiac rest period in diastolic phase.[18] The mean rest period of RCA was 212 ms (range 80–400 ms).

Table 1
Image quality scores of coronary artery segments for coronary magnetic resonance angiography acquired during a single breath-hold (BH-CMRA) and those using conventional respiratory-gated CMRA (RG-CMRA).

Coronary artery segments	Image quality scores (mean ± S.D.)		Difference
	BH-CMRA	RG-CMRA	
1	**2.9 ± 0.83**	**3.9 ± 0.27**	1.0[a]
2	**2.9 ± 1.0**	**3.6 ± 0.50**	0.79
3	1.6 ± 1.2	**2.6 ± 1.3**	0.93
4	0.64 ± 0.50	1.0 ± 1.0	0.64
5	**2.4 ± 0.63**	**3.7 ± 0.47**	1.4[a]
6	**2.2 ± 1.1**	**3.5 ± 0.52**	1.3[a]
7	**2.1 ± 0.86**	**3.1 ± 0.54**	1.0[a]
8	1.1 ± 0.62	**2.1 ± 0.73**	1.0[a]
9	1.2 ± 0.97	**2.3 ± 0.99**	1.1
10	0.57 ± 0.65	0.93 ± 0.92	0.36
11	**2.1 ± 0.77**	**3.5 ± 0.52**	1.4[a]
12	0.86 ± 0.66	1.9 ± 1.3	1.0
13	1.6 ± 0.75	**2.6 ± 0.65**	0.93
14	0.71 ± 0.73	1.8 ± 1.1	1.1
15	0.07 ± 0.27	0.21 ± 0.58	0.14

[a] Segments with significant score reduction in BH-CMRA compared to RG-CMRA after correction for multiple comparisons of segments with scores higher than 2 in RG-CMRA ($p < 0.005$). Segments with acceptable quality for clinical evaluation in BH-CMRA, i.e., scored over 2, are also indicated in bold.

Eleven subjects had rest periods less than the length of acquisition window for BH-CMRA. The scan times were 11 min and 51 s (range 6 min 34 s to 15 min 42 s) for RG-CMRA, and 34 s (range 19–44 s) for BH-CMRA.

The average scores of all the segments were 1.52 and 2.45 for BH-CMRA and RG-CMRA, respectively. The average difference was 0.93 (see Table 1 for details). Ten segments (i.e., segments 1–3, 5–9, 11, and 13) had average scores higher than 2 in RG-CMRA. Of these, BH-CMRA had scores significantly different than RG-CMRA at segments 1, 5–8, and 11 after correction for multiple comparisons ($p < 0.005$). However, in BH-CMRA, proximal segments (segments 1–2, 5–7, and 11) showed average scores over 2 (Fig 1).

Discussion

The introduction of multiple array coils has enabled 2D PI, allowing BH whole-heart coronary imaging. Conventional coil systems are typically comprised of only a few coil arrays, and noise amplifies rapidly as the acceleration factor increases. As such, the current clinical acceleration factor is 2 in one direction, as higher factors only in one direction steeply increase the g-factor and noise. In contrast, a multi-array coil system arranged in two dimensions can alleviate noise amplification.[19] PI applied simultaneously to two directions of phase- and section-encoding in 3D acquisition can diminish deterioration of signal-to-noise ratio (SNR) caused by acceleration.[13,20] The whole-heart CMRA scans a thick slab that spans multiple coil elements, and allows PI in the slice direction. Further, 3D acquisition with a large scan volume had the advantage of offsetting SNR losses caused by acceleration.[16]

RG-CMRA was acquired by continuous observation of the diaphragm position and compensating for a small amount of displacement within an acceptance window of approximately 5 mm to give a reasonable compromise between scan efficiency and image quality.[21] However, changes in respiratory pattern and depth leads to a higher gating failure, prolonging the scan time.[9] Feedback of the respiratory

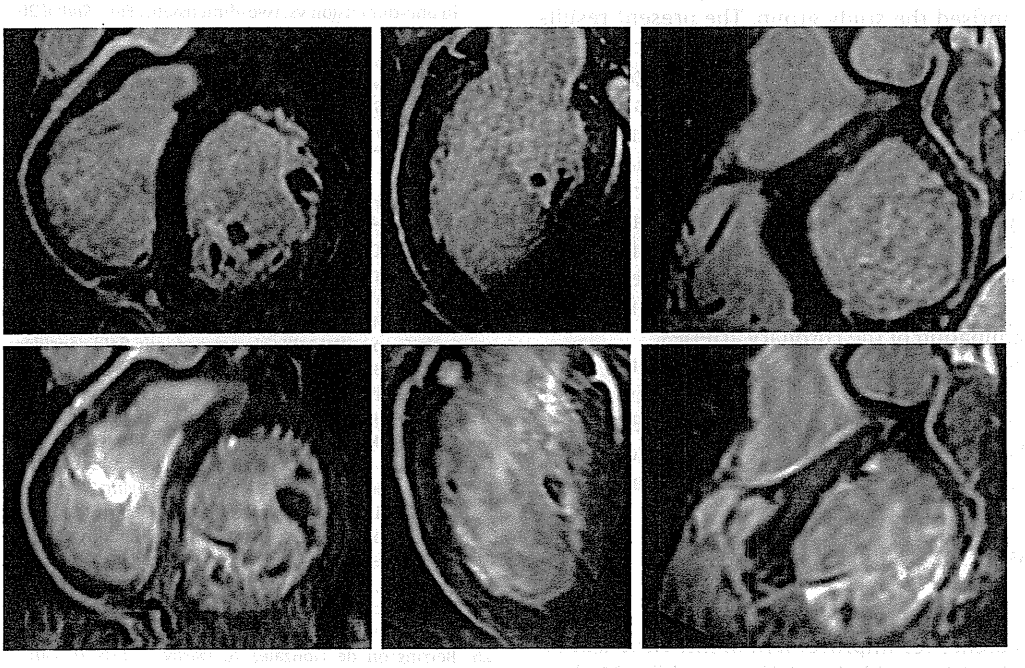

Figure 1 Visualization of CMRA using single BH and RG acquisitions. Curved planar reconstructions of the RCA (left), LAD (middle), and LCX (right) are presented for RG-CMRA (upper row) and BH-CMRA (lower row). Comparable visualization was observed between the two methods, although the images were somewhat smoothed in BH-CMRA.

patterns and depth improves efficiency,[22] although the acquisition times can still be very long. Alternatively, CMRA can be performed during a single BH, although the average scan time in the present study was as long as 34 s.

In a study of breath-holding capabilities in 50 patients, it was reported that the majority of outpatients who were not heavy smokers and who were without chronic obstructive pulmonary disease or congestive heart failure could achieve a single BH of 38 s.[23] However, breath-holding for a long duration can cause large diaphragm displacement and heart rate changes.[8] As BH-CMRA can be commonly performed clinically, this may provide a further application of CMRA as a screening tool.

In the present study, the average scores for coronary visualization were degraded in all segments, particularly at proximal segments where the RG-CMRA had average scores higher than 3. The majority of these segments had average scores greater than 2 in BH-CMRA. There are two main causes for this reduction in the scores. First, breath-hold acquisition has lower resolution, especially with respect to section thickness, and the number of sections had to be reduced in order to obtain a scan time around 30 s. Second, longer acquisition windows than the cardiac rest periods are used in BH-CMRA. Raw data acquisition was conducted from the centre to outward, although data at the *k*-space periphery are affected by cardiac motion and some image degradation was considered inevitable. As a result of these factors, the level of confidence in the present study was low. Nevertheless, BH-CMRA can be acquired in less than 1 min, and as such, the additional scan time can be ignored. Moreover, occasionally RG-CMRA acquisition fails to be completed,[22] and BH-CMRA would be used as a fail-safe for time-consuming RG-CMRA.

A potential limitation of the present study is that normal volunteers comprised the study group. The present results need to be validated in a clinical population and compared with a reference standard such as coronary angiography. Nevertheless, the results from the normal volunteers are important when considering the rapidly growing use of multidetector computed tomography (CT) coronary angiography. In a recent study, 75% of patients with acute chest pain had no significant CT findings and a final diagnosis of clinically insignificant chest pain[24]; there is also a significant risk of carcinogenesis caused by diagnostic x-rays, especially via CT.[25] The proposed BH method would facilitate the use of MR for the examination of the coronary arteries.

In summary, the present study demonstrated the capability for rapid coronary imaging within a BH using 2D PI. Although the image quality obtained was limited, BH-CMRA is feasible and easily implemented, and may be useful as an adjunct for a routine MR examinations of the heart.

Acknowledgements

This study was supported by a sponsored research program, "Researches for improvement of MR visualization (No. 150100700014)" provided to K.T. by Toshiba Medical Systems Incorporated, Japan.

References

1. Kim WY, Danias PG, Stuber M, et al. Coronary magnetic resonance angiography for the detection of coronary stenoses. *New Engl J Med* 2001;**345**:1863–9.
2. Botnar RM, Stuber M, Danias PG, et al. Improved coronary artery definition with T2-weighted, free-breathing, three-dimensional coronary MRA. *Circulation* 1999;**99**:3139–48.
3. Weber OM, Martin AJ, Higgins CB. Whole-heart steady-state free precession coronary artery magnetic resonance angiography. *Magn Reson Med* 2003;**50**:1223–8.
4. Stuber M, Weiss RG. Coronary magnetic resonance angiography. *J Magn Reson Imaging* 2007;**26**:219–34.
5. Sakuma H, Ichikawa Y, Suzawa N, et al. Assessment of coronary arteries with total study time of less than 30 minutes by using whole-heart coronary MR angiography. *Radiology* 2005;**237**:316–21.
6. Taylor AM, Keegan J, Jhooti P, et al. Differences between normal subjects and patients with coronary artery disease for three different MR coronary angiography respiratory suppression techniques. *J Magn Reson Imaging* 1999;**9**:786–93.
7. Wang Y, Grist TM, Korosec FR, et al. Respiratory blur in 3D coronary MR imaging. *Magn Reson Med* 1995;**33**:541–8.
8. Holland AE, Goldfarb JW, Edelman RR. Diaphragmatic and cardiac motion during suspended breathing: preliminary experience and implications for breath-hold MR imaging. *Radiology* 1998;**209**:483–9.
9. Taylor AM, Jhooti P, Wiesmann F, et al. MR navigator-echo monitoring of temporal changes in diaphragm position: implications for MR coronary angiography. *J Magn Reson Imaging* 1997;**7**:629–36.
10. Kim WY, Stuber M, Kissinger KV, et al. Impact of bulk cardiac motion on right coronary MR angiography and vessel wall imaging. *J Magn Reson Imaging* 2001;**14**:383–90.
11. Scott AD, Keegan J, Firmin DN. Motion in cardiovascular MR imaging. *Radiology* 2009;**250**:331–51.
12. Pruessmann KP, Weiger M, Scheidegger MB, et al. SENSE: sensitivity encoding for fast MRI. *Magn Reson Med* 1999;**42**:952–62.
13. Weiger M, Pruessmann KP, Boesiger P. 2D SENSE for faster 3D MRI. *MAGMA* 2002;**14**:10–9.
14. Buehrer M, Huber ME, Wiesinger F, et al. Coil setup optimization for 2D-SENSE whole-heart coronary imaging. *Magn Reson Med* 2006;**55**:460–4.
15. Okada T, Kanao S, Ninomiya A, et al. Whole-heart coronary magnetic resonance angiography with parallel imaging: comparison of acceleration in one-dimension vs. two-dimensions. *Eur J Radiol* 2009;**71**:486–91.
16. Niendorf T, Hardy CJ, Giaquinto RO, et al. Toward single breath-hold whole-heart coverage coronary MRA using highly accelerated parallel imaging with a 32-channel MR system. *Magn Reson Med* 2006;**56**:167–76.
17. Danias PG, McConnell MV, Khasgiwala VC, et al. Prospective navigator correction of image position for coronary MR angiography. *Radiology* 1997;**203**:733–6.
18. Wu YW, Tadamura E, Yamamuro M, et al. Evaluation of three-dimensional navigator-gated whole heart MR coronary angiography: the importance of systolic imaging in subjects with high heart rates. *Eur J Radiol* 2007;**61**:91–6.
19. Wiesinger F, Boesiger P, Pruessmann KP. Electrodynamics and ultimate SNR in parallel MR imaging. *Magn Reson Med* 2004;**52**:376–90.
20. Ohliger MA, Grant AK, Sodickson DK. Ultimate intrinsic signal-to-noise ratio for parallel MRI: electromagnetic field considerations. *Magn Reson Med* 2003;**50**:1018–30.
21. Oshinski JN, Hofland L, Mukundan Jr S, et al. Two-dimensional coronary MR angiography without breath holding. *Radiology* 1996;**201**:737–43.
22. Okada T, Kuhara S, Kanao S, et al. Facilitated acquisition of whole-heart coronary magnetic resonance angiography with visual feedback of respiration status. *Int J Cardiovasc Imaging* 2009;**25**:397–403.
23. Gay SB, Sistrom CL, Holder CA, et al. Breath-holding capability of adults. Implications for spiral computed tomography, fast-acquisition magnetic resonance imaging, and angiography. *Invest Radiol* 1994;**29**:848–51.
24. White CS, Kuo D, Kelemen M, et al. Chest pain evaluation in the emergency department: can MDCT provide a comprehensive evaluation? *AJR Am J Roentgenol* 2005;**185**:533–40.
25. Berrington de Gonzalez A, Darby S. Risk of cancer from diagnostic x-rays: estimates for the UK and 14 other countries. *Lancet* 2004;**363**:345–51.

European Journal of Radiology xxx (2011) xxx–xxx

Contents lists available at ScienceDirect

European Journal of Radiology

journal homepage: www.elsevier.com/locate/ejrad

MRI evaluation of residual tumor size after neoadjuvant endocrine therapy vs. neoadjuvant chemotherapy

Kazuna Takeda[a], Shotaro Kanao[a,*], Tomohisa Okada[a], Takayuki Ueno[b], Masakazu Toi[b], Hiroshi Ishiguro[c], Yoshiki Mikami[d], Shiro Tanaka[e], Kaori Togashi[a]

[a] Department of Diagnostic Imaging and Nuclear Medicine, Kyoto University Graduate School of Medicine, 54 Shogoin Kawaharacho, Sakyoku, Kyoto 606-8507, Japan
[b] Department of Breast Surgery, Kyoto University Graduate School of Medicine, Kyoto 606-8507, Japan
[c] Outpatient Oncology Unit, Kyoto University Graduate School of Medicine, Kyoto 606-8507, Japan
[d] Department of Diagnostic Pathology, Kyoto University Graduate School of Medicine, Kyoto 606-8507, Japan
[e] Translational Research Center, Kyoto University Graduate School of Medicine, Kyoto 606-8507, Japan

ARTICLE INFO

Article history:
Received 28 February 2011
Received in revised form 9 May 2011
Accepted 10 May 2011

Keywords:
MRI
Breast cancer
Neoadjuvant endocrine therapy
Neoadjuvant chemotherapy
Residual tumor size

ABSTRACT

Aim: To investigate if there is any difference in evaluation of residual tumor size after neoadjuvant chemotherapy (NAC) and neoadjuvant endocrine therapy (NAE).
Methods: Seventy-eight tumors in 57 patients were prospectively enrolled. Residual tumor sizes in contrast-enhanced MRI after NAC and NAE were compared with those measured on surgical specimen by using linear regression analyses. The line slope values >1 indicates overestimation by MRI. Differences in types of shrinkage patterns: concentric shrinkage (CS) and dendritic shrinkage (DS) were also investigated.
Results: Fifty lesions were treated with NAC and 28 lesions were treated with NAE. Shrinkage patterns were CS in 33 lesions and in 45 lesions. The slopes values were 0.75 ($R=0.92$) and 0.70 ($R=0.90$) for NAC and NAE, respectively, and no significant difference was observed ($p=0.46$). However, they were 1.02 ($R=0.92$) and 0.68 ($R=0.92$), respectively for CS and DS with significant difference ($p<0.01$). The difference between CS and DS was found only in a subgroup with size by MRI >20 mm.
Conclusion: Contrast enhanced MRI enabled fairly accurate measurement in NAE as well as in NAC.

1. Introduction

Neoadjuvant chemotherapy (NAC), which is conducted before surgery, is now commonly adopted to treat breast cancer [1]. Initially, neoadjuvant chemotherapy was indicated in patients with locally advanced or inflammatory breast cancers, then indication has become to include initially operable breast cancer that is not a candidate for breast conserving surgery or that would get some benefit from tumor volume reduction [2]. Advantages of this therapeutic approach are: early treatment of micrometastatic disease, assessment of tumor response to specific chemotherapeutic regimens *in vivo* and analyses of biological markers that may predict the response.

Randomized trials comparing neoadjuvant chemotherapy and postoperative adjuvant chemotherapy have shown similar survival benefit, and preoperative chemotherapy has allowed more patients to have successful breast-conserving treatment [3]. Moreover, complete pathological response of primary breast cancer to neoadjuvant chemotherapy is a surrogate marker for patient outcome [3]. Evaluation of tumor before surgery has been conducted by some modalities including mammography, ultrasound and MRI. MRI is recognized as the most reliable method for detection of residual tumor after NAC [4–7].

Recently, neoadjuvant endocrine therapy (NAE) is gradually adopted in addition to NAC [8]. NAE is considered to be another therapeutic option for a tumor that is highly sensitive to endocrine treatment, especially in elderly population [9]. NAE is often selected for cases of less aggressive cancer than NAC [10], and their similarity and difference in MRI evaluation after presurgical systemic therapies have not been much investigated and still remains to be clarified. Discrepancy was sometimes observed after NAC between assumed residual tumor size evaluated by MRI and that confirmed by resected specimen [7,11]. Patterns of shrinkage, i.e., concentric shrinkage (CS) or dendritic shrinkage (DS) [12], and status of human epidermal growth factor receptor related 2 (HER2), i.e., positive or negative [13], were reported to have some roles for correct evaluation by MRI. Confirmation on MRI evaluation of residual tumor size after NAE has large clinical importance for selection of further therapeutic options.

* Corresponding author. Tel.: +81 75 751 3760; fax: +81 75 771 9709.
E-mail address: kanaos@kuhp.kyoto-u.ac.jp (S. Kanao).

0720-048X/$ – see front matter © 2011 Elsevier Ireland Ltd. All rights reserved.
doi:10.1016/j.ejrad.2011.05.013

Table 1
Lesion characteristics: NAC vs. NAE.

	NAC lesions $n=50$	NAE lesions $n=28$	
Mean age (range)	51 (34–76)	59 (39–80)	$p<0.01$
Clinical tumor stage			$p=0.10$
T1	27 (54%)	9 (32%)	
T2	16 (32%)	17 (61%)	
T3	2 (4%)	1 (4%)	
T4	5 (10%)	1 (4%)	
Nodal status			$p=0.84$
Negative	31 (62%)	18 (64%)	
Positive	19 (38%)	10 (36%)	
Histological subtype			$p=0.04$
IDC NOS	48 (96%)	24 (86%)	
ILC	0 (0%)	1 (4%)	
IDC + ILC	1 (2%)	0 (0%)	
Metaplastic carcinoma	1 (2%)	0 (0%)	
Mucinous carcinoma	0 (0%)	3 (11%)	
Histological grade			$p<0.01$
Grade 1	3 (6%)	12 (43%)	
Grade 2	31 (62%)	14 (50%)	
Grade 3	16 (32%)	2 (7%)	
Receptor status			$p<0.01$
ER and/or PR (+) HER2 (+)	8 (16%)	0 (0%)	
ER and/or PR (+) HER2 (−)	25 (50%)	28 (100%)	
ER and PR (−) HER2 (+)	6 (12%)	0 (0%)	
ER and PR (−) HER2 (−)	11 (22%)	0 (0%)	
Ki-67 labeling index			$p<0.01$
Low (<15%)	7 (14%)	23 (82%)	
Intermediate (16–30%)	8 (16%)	2 (7%)	
High (>31%)	10 (20%)	0 (0%)	
n.a.	25 (50%)	3 (11%)	
Final pathological status			$p<0.01$
Non-CR	39 (76%)	27 (96%)	
CR	12 (24%)	1 (4%)	

Abbreviations: NAC: neoadjuvant chemotherapy; NAE: neoadjuvant endocrine therapy; n.a.: not accessed. ER: estrogen receptor; PR: progesterone receptor; HER2: human epidermal growth factor receptor related 2; IDC: invasive ductal carcinoma; NOS: not otherwise specified; ILC: invasive lobular carcinoma; CR: complete response.

Table 2
Lesion characteristics: CS vs. DS.

	CS lesions $n=33$	DS lesions $n=45$	
Mean age (range)	54 (34–80)	55 (34–76)	$p=0.58$
Clinical tumor stage			$p=0.10$
T1	13 (39%)	23 (51%)	
T2	18 (55%)	15 (33%)	
T3	1 (3%)	2 (4%)	
T4	1 (3%)	5 (11%)	
Nodal status			$p=0.89$
Negative	20 (61%)	28 (65%)	
Positive	13 (39%)	17 (35%)	
Histological subtype			$p=0.31$
IDC NOS	30 (91%)	42 (93%)	
ILC	0 (0%)	1 (2%)	
IDC + ILC	0 (0%)	1 (2%)	
Metaplastic carcinoma	1 (3%)	0 (0%)	
Mucinous carcinoma	2 (6%)	1 (2%)	
Pathological grade			$p=0.28$
Grade 1	9 (27%)	6 (13%)	
Grade 2	16 (48%)	29 (64%)	
Grade 3	8 (24%)	10 (22%)	
Ki-67 labeling index			$p=0.77$
Low (<15%)	12 (36%)	18 (40%)	
Intermediate (16–30%)	3 (9%)	7 (16%)	
High (>30%)	3 (9%)	7 (16%)	
n.a.	15 (45%)	13 (29%)	
Final pathological status			$p=0.13$
Non-CR	25 (76%)	40 (89%)	
CR	8 (24%)	5 (11%)	

Abbreviations: CS: concentric shrinkage; DS: dendritic shrinkage; ER: estrogen receptor; PR: progesterone receptor; HER2: human epidermal growth factor receptor related 2; IDC: invasive ductal carcinoma; NOS: not otherwise specified; IDC: invasive ductal carcinoma; ILC: invasive lobular carcinoma; CR: complete response.

Therefore, we made a prospective study for size evaluation of residual tumor by MRI at the end of presurgical systemic therapies of NAC and NAE, and compared the results with pathological specimen. They were analyzed in terms of differences between NAC and NAE, and also between shrinkage patterns of CS and DS.

2. Materials and methods

2.1. Patients and therapeutics

This study was approved by institutional review board and informed consent was acquired by all subjects enrolled. Seventy-nine pathologically confirmed breast cancer in 58 female patients (34–80 years old, average 54 years) were prospectively enrolled from June 2008 to February 2010, however, one tumor of progressive disease in one patient was excluded, because our study also included analysis of shrinkage cases. Therefore, 78 carcinomas in 57 patients were included for further analysis. They were treated with NAC or NAE and surgically resected thereafter at our hospital. Therapy was decided by the patient with informed consent after discussion with breast surgeons and medical oncologist. Many were based on St. Gallen Consensus Guideline 2007 or 2009 [10,14].

NAC was defined as usage of standard chemotherapeutic agents of taxane or anthracycline and their derivatives without any endocrine therapy. NAE was defined as application of endocrine therapy without chemotherapy except cyclophosphamide. The basic regimen of NAC was a combination of docetaxel (75 mg/m^2) and cyclophosphamide (600 mg/m^2) for 3–6 cycles in every 3 weeks. For NAE, letrozole was administered with addition of some

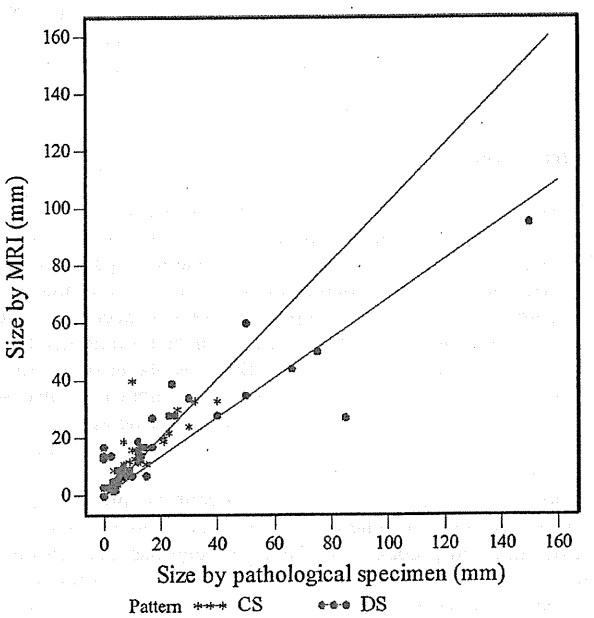

Fig. 1. Linear relationship between MRI measurement compared with that on pathological specimen. By therapeutic regimens, no significant interaction between NAC and NAE was observed ($p=0.46$). NAC: neoadjuvant chemotherapy; NAE: neoadjuvant endocrine therapy.

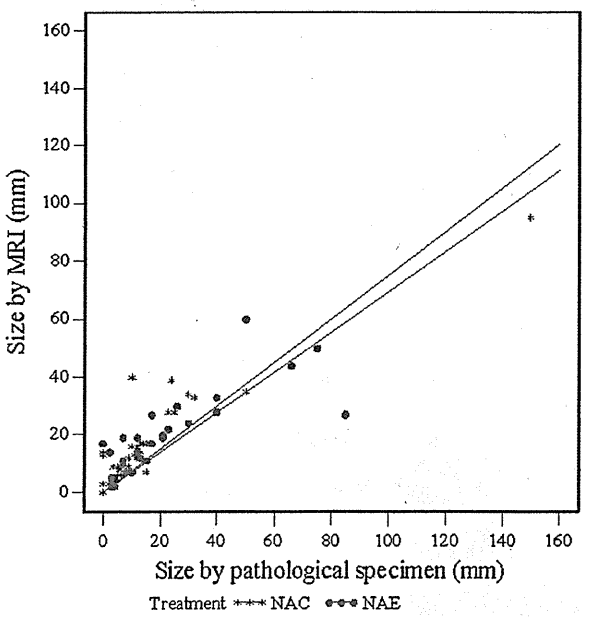

Fig. 2. Linear relationship between MRI measurement compared with that on pathological specimen. By shrinkage patterns, significant interaction between shrinkage patterns of Concentric and Dendritic was observed ($p < 0.01$).

other agents (R2) (cyclophosphamide, LH–RH analogue, etc.), when considered necessary.

2.2. MRI protocol

Using the same protocol, MRI evaluation was conducted twice before and after neoadjuvant therapies. MRI was acquired with a 3 T scanner (Magnetom Trio Tim; Siemens Medical Solutions, Erlangen, Germany) with a breast-dedicated 4-channel coil (Invivo, FL, USA) at the end of NAC or NAE. After getting pre-contrast axial T2-weighted, T1-wighted and diffusion-weighted images, fat-suppressed T1-weighted dynamic images were acquired once before and three times after Gadolinium infusion. At 0–1, 1–2 and 5–6 min after injection. The whole breasts were scanned in high temporal resolution of 1 min (3D-VIBE: TR/TE 3.8/1.48 ms, FA 15, FOV 330 mm × 330 mm, matrix 448 × 461, 2.5 mm thickness, 60 slices) in axial orientation. At 2–5 min, a scan was conducted with high spatial resolution (3D-VIBE: TR/TE 4.2/1.5 ms, FA 15, FOV 330 mm × 330 mm, matrix 448 × 412, 0.8 mm thick, 176 slices) in coronal orientation. Infused Gadolinium contrast materials were either Gadoteridol (ProHance, Eisai Inc., Tokyo, Japan) (R3) for patients under or equal to 60 kg, or Gadodiamide (Omniscan, Daiichi-Sankyo Inc., Tokyo, Japan) (R3) for patients over 60 kg, with a dose of 0.2 ml/kg power injected at the speed of 2.0 ml/s and flashed with 20 ml of saline at the same rate (R3). These two contrast agents was reported to have similar contrast effect [15].

2.3. Image analysis

Residual tumor was defined by their degree, pattern and distribution of dynamic enhancement. Enhancements at the area where a tumor existed before therapy were considered to indicate a residual tumor. Enhancements in other area were considered nonspecific except when they had definite malignant morphology or dynamic enhancement pattern. Evaluation was conducted by an experienced radiologist (Shotaro Kanao) with 10-year experience in breast MRI examination (R4). He was blinded to pathological results and other imaging results. The maximum dimension of the abnormally enhancing lesion or lesions corresponding to the known malignancy was measured using contrast-enhanced 3D-volume images reconstructed in multiple planes by using Aquarius NET Server (TeraRecon Inc., Tokyo, Japan). This maximum dimension was chosen to represent the extent of disease present in the breast. Thus, if the lesion consisted of multiple adjacent abnormalities, the maximum dimension was not the sum of their diameters, but a single measurement encompassing the lesions farthest apart [6].

The shrinkage patterns were divided into two types [11,12]. One type was concentric shrinkage (CS), which indicates the tumor shrunk from all directions toward a center. The other type was dendritic shrinkage (DS), which indicates fragmentation into multiple smaller tumor foci or uneven shrinkage of the tumor resulting in dendritic shape.

2.4. Pathological analysis

Surgical resections were conducted within 2 weeks after MRI scans. The specimen were dissected and evaluated by pathologists. They were sectioned at 5-mm intervals perpendicular to the longest axis of the specimen. Partial resection specimens were completely embedded (and in cases of mastectomy grossly visible tumor beds were also thoroughly sampled) for optimal evaluation of tumor response. Pathological complete response (pCR) was defined as no residual invasive tumor on the specimen. The pathological size was defined as longest diameter of invasive tumor.

2.5. Statistical analysis

General linear model analyses with no intercept term were conducted to examine the linear relationship between size measurements by MRI and those of pathological specimen. Regression coefficient for the slope greater than 1 meant overestimation in MRI measurements. Discrepancies between NAC vs. NAE were analyzed by fitting regression lines separately and by tests for interaction terms. Difference in CS vs. DS was also analyzed in the same manner [7]. Statistical analysis was conducted by using SAS version 9.2 (SAS Institute Inc., Cary, NC, USA). p Values less than 0.05 were considered significant.

3. Results

3.1. Pathological findings

Characteristics of patients and lesions were analyzed for differences between NAC vs. NAE, as well as CS vs. DS in terms of mean age, clinical tumor stage, nodal status, histological subtype, histological grade, receptor status, Ki-67 labeling index, and final pathological status (see Tables 1 and 2). Significant difference was observed between NAC vs. NAE in age, histological subtype, histological grade, receptor status, Ki-67 labeling index, and final pathological status. These differences were unavoidable because selection of neoadjuvant therapy linked to those parameters. No significant difference was observed between CS vs. DS.

3.2. Size evaluation with MRI vs. microscopic examination of specimen

A linear relationship was observed between size evaluation by MRI and pathological examination. The regression coefficient for slope of all tumors was 0.73 (95% confidence interval (CI): 0.65–0.80, $R^2 = 0.83$) and the relationship was statistically significant ($p < 0.01$). The regression coefficients of slopes were 0.75 (95%

Please cite this article in press as: Takeda K, et al. MRI evaluation of residual tumor size after neoadjuvant endocrine therapy vs. neoadjuvant chemotherapy. Eur J Radiol (2011), doi:10.1016/j.ejrad.2011.05.013